Layered Cobalt Hydroxysulfates with Both Rigid and Flexible Organic Pillars: Synthesis, Structure, Porosity, and Cooperative Magnetism

Apinpus Rujiwatra,[†] Cameron J. Kepert,[‡] John B. Claridge,[†] Matthew J. Rosseinsky,*[,†] Hitoshi Kumagai,[§,||] and Mohamedally Kurmoo[§]

Contribution from the Department of Chemistry, University of Liverpool, Liverpool L69 7ZD, U.K., Centre for Heavy Metals Research, School of Chemistry, University of Sydney, NSW 2006, Australia, and Institut de Physique et Chimie des Materiaux de Strasbourg, 23 rue du Loess, 67037, Strasbourg, France

Received April 17, 2001

Abstract: The synthesis and characterization of two members of a family of porous magnetic materials is described. The structures of $Co_4(SO_4)(OH)_6(C_2N_2H_8)_{0.5}\cdot 3H_2O$ and $Co_4(SO_4)(OH)_6(C_6N_2H_{12})_{0.5}\cdot H_2O$ and their thermal stability can be tailored via the choice of organic pillar. The interactions between the pillaring agent and the compositionally complex inorganic layer are discussed. The influences of two pillaring agents i.e., the flexible ethylenediamine and the relatively rigid 1,4-diazabicyclo[2,2,2]octane, on thermal stability, rigidity upon guest loss, and magnetic behavior of the pillared solids are compared. The magnetism of the pillared layered cobalt hydroxides is complex due to the influences of multiple metal sites, inter- and intralayer exchange, spin−orbit coupling, and geometrical frustration. The wide variety of potential pillars, oxyanions, and possible metal substitutions at the octahedral and tetrahedral sites offers the possibility of tailoring the magnetic and porous properties of these materials.

Introduction

Pillared layered systems (such as clays,[1−3] layered double hydroxides,[4−6] and metal phosphonates[7]) are an important class of porous materials with exchangeable guests. Given the considerable recent interest in coordination polymer frameworks, the exploration of extended inorganic layers (with their associated cooperative optical and magnetic properties) covalently linked by polydentate ligand pillars is important.[8−11] In this paper, we demonstrate both reversible guest sorption−desorption and cooperative magnetism in two-dimensional extended inorganic arrays rigidly or flexibly pillared by organic bidentate linkers.

Recently, we communicated the pH-controlled hydrothermal synthesis and structural characterization of $Co_4(SO_4)(OH)_6(C_2N_2H_8)_{0.5}\cdot 3H_2O$[12] (CSEN hereafter), a novel type of layered hydroxide derived from organic pillaring of the namuwite[13,14] (basic zinc sulfate[15]) structure. The CSEN framework consists of $Co_3(SO_4)(OH)_4\cdot Co(OH)_2$ layers with the pillaring ethylenediamine molecules linking adjacent layers via tetrahedral cobalt ions. CSEN undergoes reversible dehydration−hydration upon the loss of interlayer water and exhibits cooperative magnetism with dominant antiferromagnetic coupling at low temperatures. The triangular magnetic lattice and potential for ferromagnetic Co−O−Co superexchange[16] in the array of edge-sharing octahedra prompts further exploration of these phenomena, given the recent interest in organic−inorganic magnets.[17−27]

[†] University of Liverpool.
[‡] University of Sydney.
[§] Institut de Physique et Chimie des Materiaux de Strasbourg.
[||] On leave from Applied Molecular Science, Institute of Molecular Science, Nishigounaka, 38 Myoudaiji, Okazaki 444-8585, Japan.

(1) Burch, R. *Catal. Today* **1988**, *2* (2,3), 185.
(2) Figueras, F. *Catal. Rev.-Sci. Eng.* **1988**, *30* (3), 457.
(3) Ohtsuka, K. *Chem. Mater.* **1997**, *9*, 2039.
(4) Newman, S. P.; Jones, W. *New J. Chem.* **1998**, *22* (2), 105.
(5) Wang, J. D.; Serrette, G.; Tian, Y.; Clearfield, A. *Appl. Clay Science* **1995**, *10*, 103.
(6) Steven, P.; Jones, N.; Jones, W. *J. Solid State Chem.* **1999**, *148*, 26.
(7) Alberti, G.; Costantino, G.; Dionigi, C.; Murciamascaros, S.; Vivani, R. *Supramol. Chem.* **1995**, *6*, 29.
(8) O'Hare, D. *New J. Chem.* **1994**, 18, 989.
(9) Eddaoudi, M.; Li, H.; Yaghi, O. M. *J. Am. Chem. Soc.* **2000**, 122, 1391.
(10) O'Keeffe, M.; Eddaoudi, M.; Li, H.; Reineke, T.; Yaghi, O. M. *J. Solid State Chem.* **2000**, *152*, 3.
(11) Cheetham, A. K.; Ferey, G.; Loiseau, T. *Angew. Chem., Int. Ed.* **1999**, *38*, 3268.
(12) Rujiwatra, A.; Kepert, C. J.; Rosseinsky, M. J. *Chem. Commun.* **1999**, 2307.
(13) Groat, L. A. *Am. Mineral.* **1996**, *81*, 238.
(14) Bevins, R. E.; Turgoose, S.; Williams, P. A. *Mineral. Mag.* **1982**, *46* (338), 51.
(15) Bear, I. J.; Grey, I. E.; Madsen, I. C.; Newnham, I. E.; Rogers, L. J. *Acta Crystallogr., Sect. B* **1986**, *B42*, 32.
(16) Goodenough, J. B. *Magnetism and the chemical bond*; Interscience: New York, 1963.
(17) Kurmoo, M. *Chem. Mater.* **1999**, *11*, 3370.
(18) Kurmoo, M. *Philos. Trans., R. Soc. London A* **1999**, *357*, 3041.
(19) Tamaki, H.; Zhong, X. J.; Matsumoto, N.; Kida, S.; Koikawa, M.; Achiwa, N.; Hashimoto, Y.; Okawa, H. *J. Am. Chem. Soc.* **1992**, *114*, 6974.
(20) Bayly, S.; McCleverty, J. A.; Ward, M. D.; Gatteschi, D.; Totti, F. *Inorg. Chem.* **2000**, *39*, 1288.
(21) Francese, G.; Romero, F. M.; Neels, A.; Stoeckli-Evans, H.; Decurtins, S. *Inorg. Chem.* **2000**, *39*, 2087.
(22) Turner, S. S.; Day, P.; Abdul Malik, K. M.; Hursthouse, M. B.; Teat, S. J.; MacLean, E. J.; Martin, L.; French, S. M. *Inorg. Chem.* **1999**, *38*, 3543.
(23) Benard, S.; Yu, P.; Audiere, J. P.; Riviere, E.; Clement, R.; Guilhem, J.; Tchertanov, L.; Nakatani, K. *J. Am. Chem. Soc.* **2000**, *122*, 9444.
(24) Triki, S.; Berezovsky, F.; Pala, J. S.; Coronado, E.; Gomez-Garcia, C. J.; Clemente, J. M.; Riou, A.; Molinie, P. *Inorg. Chem.* **2000**, *39*, 3771.
(25) Price, D. J.; Lionti, F.; Ballou, F.; Wood, P. T.; Powell, A. K. *Philos. Trans., R. Soc. London A* **1999**, *357*, 3099.
(26) Miller, J. S. *Inorg. Chem.* **2000**, *39*, 4392.
(27) Choudhury, A.; Natarajan, S.; Rao, C. N. R. *J. Solid State Chem.* **2000**, *155*, 62.

10.1021/ja0109848 CCC: $20.00
Published on Web 10/05/2001

In this paper, we use the rigid 1,4-diazabicyclo[2,2,2]octane (DABCO) to prepare the layered-phase $Co_4(SO_4)(OH)_6$-$(C_6N_2H_{12})_{0.5}.H_2O$ (CSDAB). A detailed comparison of the structural, sorptive, and magnetic properties of the two closely related phases demonstrates the controlling influence of the rigidity of the organic pillar on the chemistry and its subtle but important influence on the cooperative magnetism.

Experimental Section

Synthesis. Two similar synthetic routes to CSDAB were developed: route 1 involves dissolving $Co(NO_3)_2{\cdot}6H_2O$ (98% Aldrich, 1.273 g) and 1,4-diazabicyclo[2,2,2]octane (98% Aldrich, 0.337 g) in freshly prepared sulfuric acid solution (0.44 cm^3 of concentrated sulfuric acid (98% Aldrich) in 9.00 cm^3 of deionized water) to give a clear pink solution with molar composition $Co(NO_3)_2{\cdot}6H_2O/0.75DABCO/2H_2SO_4/114H_2O$. KOH aqueous solution (4.40 $cm^3$of a 6 M solution) was then added, affording a blue amorphous solid precipitate. After stirring for 30 min, the pH of the supernatant solution measured with an ion-selective field effect transistor (ISFET) electrode was 8.3(1). The reaction was performed (200 °C 30 h, autogenous pressure) in a sealed hydrothermal bomb fitted with a Teflon liner (22 cm^3 volume and 70% fill factor), and cooled to room temperature at a rate of 0.40 °C min^{-1}. Under the conditions used for the synthesis of CSEN (150 °C, 3 days), an amorphous phase was obtained. The product was then recovered by filtration and washed with deionized water and acetone, giving a pure blue polycrystalline product. The quality of the product was very sensitive to small variations of the reaction composition, temperature, and cooling rate. For example, contamination with the dense phase $K_2[Co_3(SO_4)_3(OH)_2(H_2O)_2]$[28] occurred when the reaction was cooled at a rate of less than 0.4 °C min^{-1}. To obtain crystals suitable for single-crystal X-ray studies, aluminum isopropoxide ($Al[(CH_3)_2CHO]_3$, 0.1276 g) was added as a mineralizer, combined with quenching the reaction to room temperature rather than slow cooling. This, however, led to an unidentified impurity in the bulk material.

Route 2 is effective on a larger scale: $Co(NO_3)_2{\cdot}6H_2O$ (3.0 g) and Na_2SO_4 (1.5 g) were dissolved in ~40 mL of distilled water, and DABCO (0.77 g) was then added followed by NaOH solution (0.26 g in 40 mL of distilled water) while stirring. The reaction mixture was treated in a PTFE-lined autoclave at 170 °C for 3 days. The autoclaves were then placed in a water bath and cooled to room temperature. Blue microcrystals were obtained and shown to be identical to those prepared by route 1 by powder X-ray diffraction.

CSEN is also accessible by two routes: (1) A mixture of $Co(NO_3)_2{\cdot}6H_2O$, H_2SO_4, ethylenediamine, KOH, and water with the molar ratio of 1:2:0.6:5.4:100, respectively, was treated under hydrothermal conditions at 150 °C for 3 days, yielding blue platelike crystals of CSEN. (2) $Co(NO_3)_2{\cdot}6H_2O$ (3.0 g) and Na_2SO_4 (0.75 g) were dissolved in distilled water (~40 mL), and ethylenediamine (~1.38 g) was added. The mixture was stirred and then an aqueous solution of NaOH (0.41 g in 40 mL of distilled water) was added. The mixture was placed in a Teflon-lined autoclave and heated to 170 °C for 3 days followed by cooling to room temperature. Blue microcrystals are obtained. The crystals were washed with water and acetone and dried under air.

X-ray Crystallography. The purity and crystallinity of the bulk samples was characterized by powder X-ray diffraction using a Phillips diffractometer with Cu Kα radiation and a secondary graphite monochromator, and a Siemens D500 diffractometer employing monochromatized Co Kα1 radiation. The measurements were performed at ambient conditions in the $3 \le 2\theta/\text{deg} \le 70$ range.

A single crystal of CSDAB 0.200 × 0.050 × 0.030 mm^3 in size (obtained as described in route 1 above) was examined on a Bruker AXS Smart CCD diffractometer equipped with a silicon 111 monochromator ($\lambda = 0.689$ Å) and Oxford Cryostream on Station 9.8[29] of the Daresbury Synchrotron Radiation Source at 150(2) K under a cooled N_2 stream. The Bruker suite of local programs at Daresbury was used to process the collected data. The SADABS area detector absorption correction was applied to the collected data.[30] The crystal structure was solved and refined by a combination of direct and Fourier methods (SHELXS-86[31] and SHELXL-97[32]). The systematic absences indicated *P*3*c*1, P$\bar{3}$*c*1, *P*6$_3$*mc*, P$\bar{6}$2*c*, or *P*6$_3$/*mmc* as possible space groups, and these were consequently employed in solving the structure. The common feature of the solutions from direct methods using the suggested space groups was the layered structure. However, only the P$\bar{3}$***c***1 space group gave a chemically sensible structure with acceptable agreement indices and a stable refinement. Every non-hydrogen atom in the asymmetric unit was located by direct methods. The tetrahedral cobalt, sulfate group, nitrogen atoms, and water molecule were located on 3-fold axes. Hydrogen atoms were located using the riding model, except the H(2) atom bound to O(2), which was assigned from the electron density map. No hydrogen atoms were added to the water site due to its high degree of disorder. We present a model with anisotropic refinement of the water molecule lying on the 3-fold axis. Isotropic refinement with the water oxygen atom lying away from the 3-fold axis, as found in CSEN, with one-third occupation gave similar refinement indices. This suggests that there may be 3-fold disorder of this molecule with differing extents of hydrogen bonding to its three neighboring framework hydroxyls. Elemental analysis revealed that aluminum was not incorporated into the crystal from the mineralizer.

Thermal Analysis. Thermogravimetric and differential thermal analysis (TG/DTA) data were collected on a Seiko SII-TG/DTA 6300 instrument for $20 \le T/°C \le 800$ under helium flow with a heating rate of 2 °C min^{-1}. The gas outlet was connected to a Hiden HPR 20 RGA mass spectrometer (MS) to characterize the liberated species. The spectrometer was employed with 70-V electron bombardment energy and 10^{-6} Torr gas pressure.

TG/DTA-MS was also used to monitor the reversibility of the dehydration−hydration reaction. After fully dehydrating CSDAB at 220 °C under a flow of He, the sample was then cooled to room temperature under a water-saturated He flow at a cooling rate of 10 °C min^{-1} followed by 3-h exposure to water vapor at room temperature.

The CO_2 uptake of the amorphous phase after the loss of the sulfate groups was explored. The amorphous phase of CSDAB was prepared under a flow of He at 360 °C, where the sulfate groups were completely lost, followed by exposure of the as-prepared phase to the flow of CO_2 gas on cooling to room temperature, and followed by another 3 h of annealing at this temperature.

Vibrational Spectroscopic Analysis. FTIR data were collected with Nicolet Magna-IR 560 and Mattson FTIR spectrometers in the mid-IR region (4000−400 cm^{-1}) with 0.50 cm^{-1} resolution. The sample films were prepared in both Nujol and Fluorolube mulls and as dispersed particles on a KBr plate.

UV−Visible Spectroscopy. UV−visible spectra were recorded on a Hitachi U-3000 spectrometer on samples dispersed in glycerol and held between two quartz plates.

Magnetic Measurements. Detailed ac and dc magnetization data were collected using Quantum Design MPMS-SQUID magnetometers on monophasic samples of CSEN and CSDAB. Zero-field cooled (ZFC) and field cooled (FC) dc data were recorded in applied fields of 1000, 100, and 10 Oe over the temperature range $5 \le T/K \le 300$. Low-field dc measurements were performed on warming and cooling the sample in 0.58 Oe after ZFC to 2 K. The influence of guest loss on the magnetic behavior was investigated by measuring the magnetization of both CSDAB and CSEN on heating to 400 K and subsequent cooling over the range $200 \le T/K \le 400$ in 25 Oe. Field-cooled magnetization measurements in external fields both less than and larger than the critical metamagnetic field were conducted on cooling from 300 K. Isothermal magnetization data were collected at $T < 100$ K, in fields of up to 50 kOe. Ac measurements were performed on cooling the sample in a field of 1 Oe oscillating at 20 Hz.

(28) Effenberger, H.; Langhof, H. *Monatsh. Chem. Verw. Teile Anderer Wiss.* **1978**, 165.

(29) Clegg, W.; Elsegood, M. R. J.; Teat, S. J.; Redshaw, C.; Gibson, V. C. *J. Chem. Soc., Dalton Trans.* **1998**, 3037.

(30) Area-Detector Absorption Correction. Siemens Industrial Automation, Inc.: Madison WI, 1996.

(31) Sheldrick, G. M. *Crystallographic Computing 3*; Oxford University Press: Oxford, U.K., 1985.

(32) Sheldrick, G. M. *SHELXL-97: Program for refinement of crystal structure*, Universität Gottingen, Gottingen, Germany, 1997.

Table 1. Summary of Single Crystal X-ray Data and Refinement Results for CSDAB

formula	$Co_4(SO_4)(OH)_6(C_6N_2H_{12})_{0.5}\cdot H_2O$
formula weight	507.94
crystal description	blue platelet
crystal size/mm^3	0.200 × 0.050 × 0.030
crystal system	trigonal
space group	*P*3c1
a/Å	8.3030(3)
c/Å	20.3340(10)
unit cell volume/Å^3	1214.01(9)
Z	3
ρ_{calc}/g cm^{-3}	2.150
T/K	150(2)
radiation (λ/Å)	Synchrotron (0.68900)
μ/mm^{-1}	4.051
θ_{min}, θ_{max}	2.75, 29.18
total data collected	7609
unique data	1153
observed data	831
R_{int}	0.0623
parameters refined	65
restraints no.	0
goodness of fit	1.074
R, R_w(all data)	0.0817, 0.1458
R, R_w($I > 2\sigma(I)$)	0.0576, 0.1388

Temperature-dependent isothermal magnetization measurements were recorded on a Princeton Applied Research VSM operating at 110 kHz and a home-built cryostat operating in the temperature range 4−300 K and fields of up to 18 kOe.

High-Temperature X-ray Diffraction. The dehydration−hydration process was studied by in situ X-ray diffraction at high temperature. The experiments were performed on a Siemens D5005 X-ray diffractometer with Cu Kα1 (λ = 1.540 59 Å) radiation equipped with a Gobel mirror multilayer monochromator and an Anton-Parr HTK1200 high-temperature cell under flowing He and water-saturated He for dehydration and hydration, respectively.

Results

Synthesis. The tetrahedral−octahedral−tetrahedral (T−O−T) layer structure compounds only form under alkaline pH, as this is required to stabilize tetrahedral Co^{II}. Acid synthesis conditions result in the formation of $CoSO_4\cdot xH_2O$ phases containing octahedral Co^{II}.

Structural and Spectroscopic Characterization of CSDAB and CSEN. The crystallographic details of CSDAB are summarized in Table 1, and a section of the structure is shown in Figure 1a. The atomic parameters are listed in Table S1 (Supporting Information). The studied crystal was confirmed to be a representative of the bulk material synthesized in the absence of aluminum isopropoxide by elemental analysis data (C, 6.68; H, 2.72; N, 2.66; Co, 45.94; S, 5.84), which are in good agreement with the values calculated from the crystallographic formula $Co_4SO_4(OH)_6(C_6N_2H_{12})_{0.5}\cdot H_2O$ (C, 7.09; H, 2.78; N, 2.76; Co, 46.4; S, 6.31). Every peak in the powder X-ray diffraction pattern was indexed and refined in the trigonal space group P$\bar{3}$*c*1 (a = 8.303(3) Å, c = 20.334(1) Å, V = 1214.0(6) Å^3), indicating the absence of any crystalline impurity. Complementary data for CSEN are shown for comparison.

The structure of $Co_4(SO_4)(OH)_6(C_6N_2H_{12})_{0.5}\cdot H_2O$ (CSDAB) retains the organic pillaring of inorganic octahedral/tetrahedral cobalt hydroxysulfate layers found in CSEN. (Figure S1, Supporting Information) It is constructed from the stacking of T−O−T layers, as shown in Figure 2. The layers are formed by edge-sharing Co^{II} octahedra regularly decorated by tetrahedral Co^{II} located above and below the layer at the vacant octahedra present at every sixth site. Layer neutrality is completed by

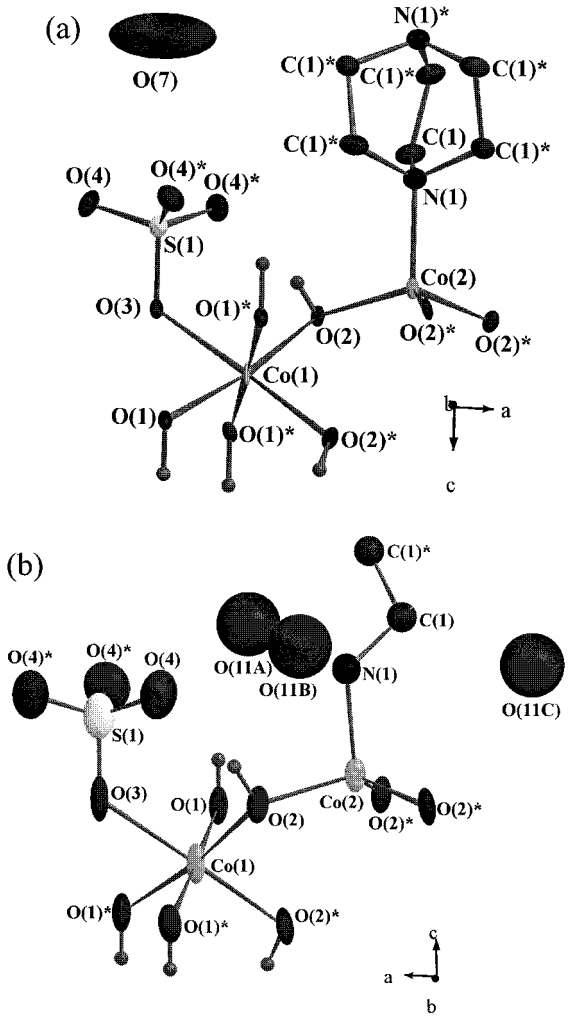

Figure 1. Local coordination environments of (a) CSDAB and (b) CSEN showing thermal ellipses of 70% probability with numbering schemes for comparison.

sulfate groups, which project out from the layer and share oxygen atoms with three neighboring CoO_6 octahedra, giving the layer composition $Co_3^{oct}(SO_4)(OH)_4\cdot Co^{tet}(OH)_2$. The sulfate group coordinates to the layer in a manner similar to the SiO_4 unit in phyllosilicates.[33−35] The coordination at the tetrahedral metal site consists of three basal hydroxide anions, with the apical site occupied by an amino group of the DABCO ligand, which connects adjacent T−O−T layers.

A marked difference between the structure of CSDAB and that of CSEN is the doubling of the *c* axis due to the orientational order of the DABCO pillars and correlated sulfate ordering within the T−O−T layers, discussed in detail later. The DABCO-pillared T−O−T layers form a three-dimensional framework with interconnected channels running along the *a* and *b* axes. The estimated size of the opening of the channel excluding the van der Waals radii of the surrounding atoms is 2.54 × 2.13 Å^2. This corresponds to 5.0% potential solvent accessible volume (60.7 Å^3/unit cell volume of 1214.0 Å^3),[36] which is occupied by a water molecule.

Despite the fact that interatomic distances for the inorganic components of the structures of CSDAB and CSEN differ by

(33) De Fonseca, M. G.; Silva, C. R.; Barone, J. S.; Airoldi, C. *J. Mater. Chem.* **2000**, *10*, 789.
(34) De Fonseca, M. G.; Airoldi, C. *J. Mater. Chem.* **2000**, *10*, 1457.
(35) Fukushima, Y.; Tani, M. *Bull. Chem. Soc. Jpn.* **1996**, *69*, 3667.
(36) Spek, A. L.; van der Sluis, P. *Acta Crystallogr.* **1990**, *A46*, 194.

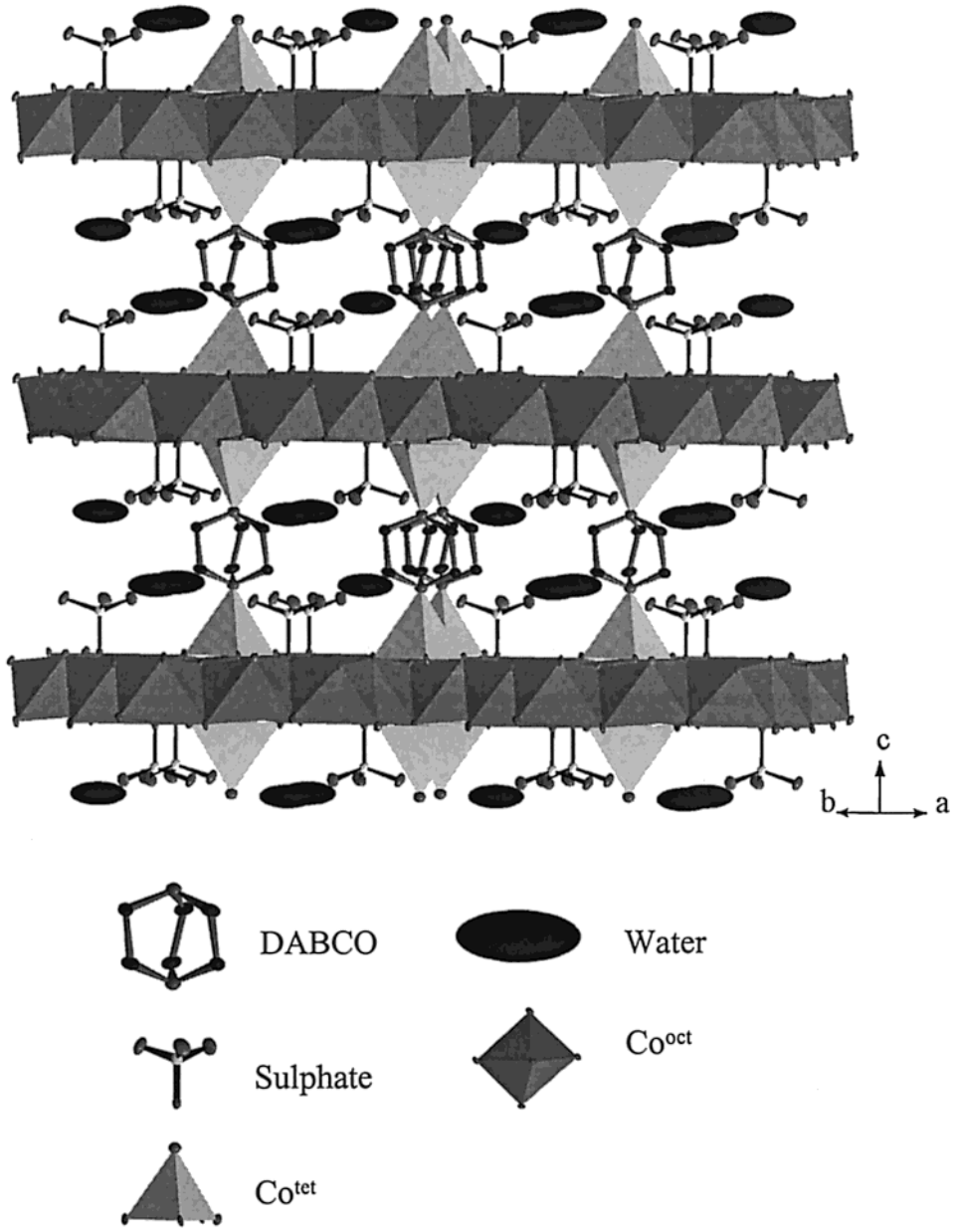

Figure 2. Tetrahedral−octahedral−tetrahedral (T−O−T) cobalt hydroxide layers of $Co_4(SO_4)(OH)_6(C_6N_2H_{12})_{0.5}\cdot H_2O$ connected to each other by DABCO pillars through the tetrahedral cobalt ions, with sulfate groups projecting into the interlayer gallery. Alternate layers are related by $\bar{3}$ symmetry to give a stacking sequence ABA (in contrast, in CSEN (Figure S1, Supporting Information), the layers are related by translation to give an AAA sequence).

less than 1%, the refined geometries of the ethylenediamine and DABCO pillars are significantly different. The N···N distance in CSDAB (2.623(1) Å) is substantially shorter than that in CSEN (3.103(1) Å) with a smaller Co(2)−N(1)−C(1) angle (111.8(4) and 122.7(2)° for CSDAB and CSEN, respectively). Selected bond lengths and angles for CSDAB and CSEN are shown in Table 2. These differences in the geometry of the organic pillars explain why the *c* axis for CSDAB is less than double that of CSEN. It should also be noted that the refinement of chemically sensible C−N distances in the case of CSEN required restraints (C−N = 1.48(2) Å).

The UV−visible spectra of both CSEN and CSDAB are identical (Figure S2, Supporting Information), reflecting the similar metal coordination environments. Three bands consistent with the coexistence of both octahedral and tetrahedral geometries in the structure were observed. The pair of transitions at 630 and 583 nm arise from the $^4A_2(P) \rightarrow {}^4T_1(P)$ transition of $Co^{II(tet)}$, and the broad band at 490 nm arises from an overlap of the $^4T_{1g}(F) \rightarrow {}^4A_{2g}(P)$ and $^4T_{1g}(F) \rightarrow {}^4T_{1g}(P)$ of $Co^{II(oct)}$.

The FTIR spectra (Figure S3, Supporting Information) reveal characteristic C−H bending modes in CSDAB and CSEN at 1467 (w) and 1387 (w) cm^{-1}, which disappear when TGA and analytical data indicate that the organic pillars are lost. The hydroxide stretches are found at 3592 (CSDAB) and 3610 cm^{-1} (CSEN). The H_2O-derived OH stretch is at 3310 cm^{-1} (CSDAB), but for CSEN overlaps with the amine N−H bands. The widths of the bands are consistent with hydrogen bonding involving the water and hydroxide units. The HOH bend is at 1625 and 1600 cm^{-1}. The SO_4 bands are at 1164 (asymmetric stretch), 990 (symmetric stretch), 670 (bend), and 460 cm^{-1} (deformation). The presence of both symmetric and asymmetric stretching bands confirms the deviation from the T_d point group of the SO_4^{2-} unit. The position and intensity of the observed bands in the CSDAB and CSEN spectra are similar, but their

Table 2. Selected Bond Lengths and Angles for CSDAB and CSEN

	CSDAB	CSEN		CSDAB	CSEN
		Bond Lengths/Å			
Co(1)−O(1)	2.086(4) × 3	2.063(6) × 3	Co(2) − N(1)	2.049(8) × 1	2.012(19) × 1
Co(1)−O(2)	2.105(15) × 2	2.102(7) × 2	S(1) − O(3)	1.542(6) × 1	1.558(15) × 1
Co(1)−O(3)	2.236(3) × 1	2.257(8) × 1	S(1) − O(4)	1.472(4) × 3	1.456(9) × 3
Co(2)−O(2)	1.960(4) × 3	1.958(6) × 3	N(1) − C(1)	1.501(7) × 1	1.48(2) × 1
Co(2)···Co(2)	10.453(1)	10.519(2)	N(1)···N(1)*	2.623(1)	3.103(1)
		Bond Angles/deg			
O(1)−Co(1)−O(2)	98.09(16)	97.7(3)	O(3)−S(1)−O(4)	107.37(19)	108.0(4)
O(1)−Co(1)−O(3)	81.98(11)	82.82(19)	Co(1)−O(2)−Co(2)	120.96(22)	121.1(3)
O(2)−Co(1)−O(3)	89.44(11)	88.8(3)	Co(1)−O(3)−S(1)	123.59(2)	124.4(3)
O(2)−Co(2)−N(1)	105.13(13)	102.64(96)	Co(2)−N(1)−C(1)	111.80(40)	122.7(2)
O(2)−Co(2)−O(2)	117.20(2)	113.52(24)			

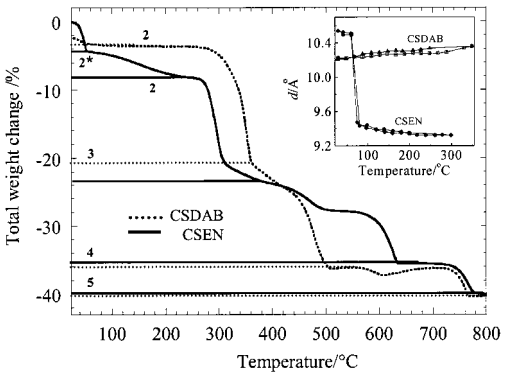

Figure 3. TGA curves showing changes for CSDAB (dotted line) and CSEN (solid line) on heating from room temperature to 800 °C at a heating rate of 2 °C/min under a flow of helium. The horizontal lines represent steps in weight losses labeled by **2**−**5** of CSDAB (dotted line) and CSEN (solid line). The corresponding variation of the interlayer spacing with temperature in CSEN and CSDAB is shown in the inset: ●, CSEN-dehydration; ◆, CSEN-hydration; ⊞ CSDAB-dehydration; and ▲, CSDAB-hydration. The **2*** composition for CSEN is a partly dehydrated phase which arises from the loss of 50.6% of the water of crystallization.

Table 3. Calculated Total Weight Losses Compared with the Observed Values for CSDAB and CSEN Corresponding to Figure 3

	CSDAB		CSEN	
phase[a]	% obsd	% calcd	% obsd	% calcd
2	3.7	4.5	8.3	7.9
3	20.5	20.2	23.3	23.8
4	36.1	35.0	35.6	36.9
5	40.0	38.7	39.8	40.5

[a]Phases: **1**, $Co_4(SO_4)(OH)_6(pillar)_{0.5}\cdot xH_2O$; **2**, $Co_4(SO_4)(OH)_6(pillar)_{0.5}$; **3**, $Co_4O(OH)_6(pillar)_{0.5}$; **4**, $Co_4O(OH)_6$; **5**, Co_2O_3 in CSEN; and a mixture of Co_3O_4 and CoO in CSDAB. *Pillar* is DABCO and ethylenediamine, and $x = 1$ and 3 in CSDAB and CSEN, respectively.

widths are reduced in the CSDAB case, indicating less disorder in the structure, which is consistent with the crystallographic data.

Thermal Properties. Thermogravimetric analysis showed CSDAB undergoes four major weight losses (Figure 3 and Table 3) under flowing helium over the range $20 \le T/°C \le 800$. The water of crystallization was readily lost under the gas flow even at room temperature and observed as the first weight change of 3.7% (calculated 4.5%) in the TGA curve, calculated from the integrated area of the first-derivative mass change. The difference between observed and calculated values is due to the loss of water before the measurement commenced. A peak in the mass spectrum at an *m*/*z* ratio of 18 amu identifies the liberated species as water. The weight remained constant in the temperature range 80−280 °C, indicating that this fully dehydrated phase **2** is stable to 280 °C. Between $280 \le T/°C \le 360$, a 20.5% weight loss was observed together with a characteristic peak of SO_3 (***m***/***z*** 80 amu) in the mass spectrum. This is attributed to the loss of the sulfate groups (calculated 20.2%), leading to the collapse of the structure, and a material **3** shown by X-ray diffraction to be amorphous. Heating to temperatures exceeding 360 °C led to the loss of the DABCO molecule comprising the third stage **4** in TGA curves with 36.1% (calculated 35.0%) mass decrease. This was confirmed by the appearance of the ion fragments of the DABCO molecules at *m*/*z* 28 and 64 amu and the disappearance of the methylene characteristic vibrational peaks at 1467 and 1387 cm^{-1}. The final 40.0% (calculated 38.7%) mass loss occurred on heating above 720 °C leading to stage **5**, a mixture of CoO and Co_3O_4.

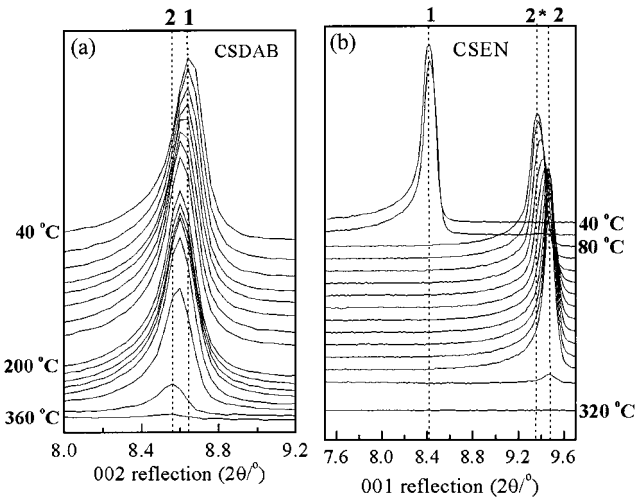

Figure 4. In situ X-ray powder diffraction patterns (Cu Kα) showing the evolution with temperature of the first intense Bragg reflection corresponding to the interlayer separation for the (a) CSDAB and (b) CSEN phases. The temperature interval between successive patterns is 20 °C. The vertical dotted lines indicate the peak maxima from the hydrated and dehydrated (**2***, **2**) phases.

Only the first weight loss process (forming **2**) is reversible. Replacement of the sulfate groups lost in step **3** by carbonate was attempted by passing CO_2 over the sample after the SO_3 loss, but no significant mass uptake was observed.

A major difference is observed during the loss of water between the CSDAB and CSEN phases. The loss of intergallery water from CSEN occurs via the intermediate **2*** phase, which corresponds to the loss of 50.6% of the interlayer water.

Dehydration−Hydration. The 002 reflection (Figure 4a) was used to follow the effect of dehydration on the interlayer spacing of CSDAB, which gradually increased from 10.17(1) to 10.27(2) Å on heating from 20 to 200 °C (Figure 3 inset). The fully dehydrated CSDAB phase **2** is obtained at 80 °C

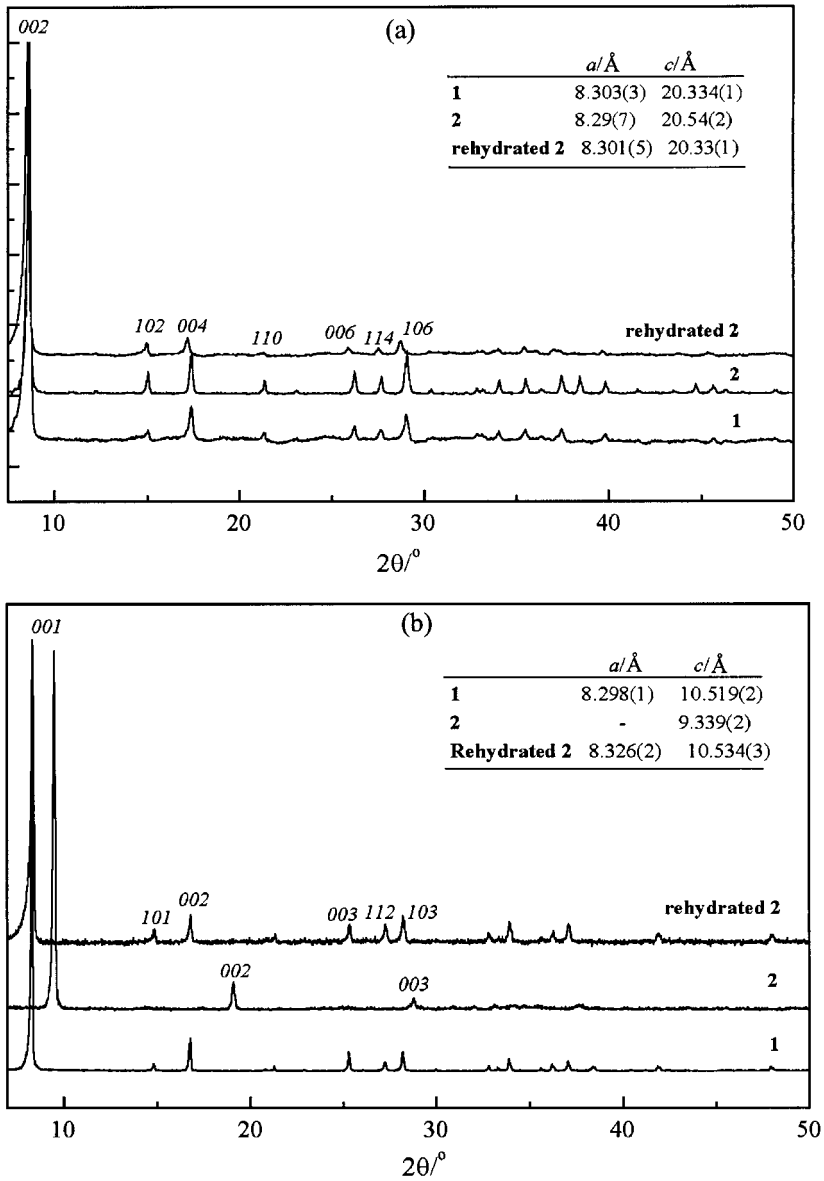

Figure 5. Powder X-ray diffraction patterns showing the reversibility of dehydration−hydration for (a) CSDAB and (b) CSEN. The latter loses the *hkl*; *h* or $k \neq 0$ reflections on dehydration indicating the loss of order between successive layers in the *xy* plane due to layer slippage. In both cases, as-synthesized, dehydrated and rehydrated phases are labeled with **1**, **2,** and rehydrated **2**, respectively, and the data for **2** were collected at 200 °C.

according to the TGA data. This is consistent with the absence of any large change to the *c* axis above 80 °C, the minor increase observed being attributable to thermal expansion. The equivalent data (Figure 4b) show that the interlayer spacing in CSEN decreases much more markedly upon dehydration.

Dehydration−hydration for CSDAB is fully reversible as demonstrated by TG/DTA-MS (Figure S4, Supporting Information) and powder X-ray diffraction. The uptake of the water by the dehydrated phase of CSDAB was shown by TGA to be 3.6%. which is consistent with the weight loss on dehydration, indicating the amounts of water lost and regained are the same. Figure 5a shows complete powder X-ray diffraction patterns of the as-prepared (**1**), dehydrated (**2**), and the rehydrated CSDAB (rehydrated **2**) phases. The data for **2** were collected in situ at 200 °C. The rehydrated phase of CSDAB could be indexed in $P\bar{3}c1$ with cell parameters $a = 8.301(5)$ Å and $c = 20.33(1)$ Å, which are in very good agreement with the starting hydrated material. Elemental analysis for the rehydrated phase was also in good agreement with the postulated formula (Observed: C, 6.76; H, 2.50; N, 2.76; Co, 47.05; S, 6.32. Calculated: C, 7.09; H, 2.78; N, 2.76; Co 46.4; S, 6.31). Dehydrated CSDAB has refined cell parameters $a = 8.29(7)$ Å, $c = 20.54(2)$ Å, and $\boldsymbol{V} = 1222.75(1)$ Å^3 and retains the same systematic absences as the as-synthesized material, which is consistent with retention of the $P\bar{3}c1$ space group symmetry. With heating to 300 °C, the interlayer spacing of the dehydrated phase increases by 0.10(2) Å, resulting in an overall increase of the cell volume of 9 Å^3. The corresponding powder patterns for CSEN show the disappearance of *hkl*, *h* or $k \neq 0$, reflections in the dehydrated powder pattern, leaving only the 00l reflections, demonstrating that only the periodicity along the interlayer direction is retained (Figure 5b), The disappearance of *hkl*, *h* or $k \neq 0$, reflections in the CSEN dehydrated powder pattern is in contrast to CSDAB in which these reflections were retained after dehydration, showing that the pillar rigidity of DABCO is essential for maintaining three-dimensional long-range order upon water loss.

Magnetic Behavior. Both the CSEN and CSDAB phases display susceptibility maxima and irreversibility at low temperatures consistent with complex magnetic ordering. The

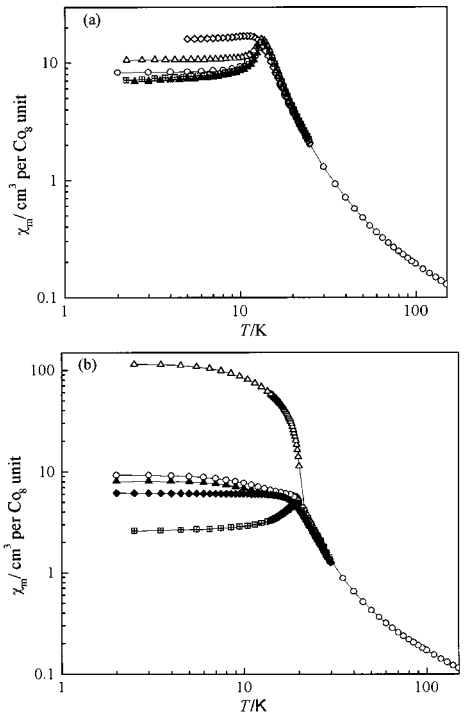

Figure 6. Magnetization data as a function of temperature for (a) CSEN and (b) CSDAB under an ac-applied field of 1 (⊞) Oe and dc-applied fields of 0.58 Oe under both field cooled (△) and zero-field cooled (▲) conditions, 100 Oe (○), 1000 Oe (◇) and 3000 Oe (◆) (field cooled in all cases).

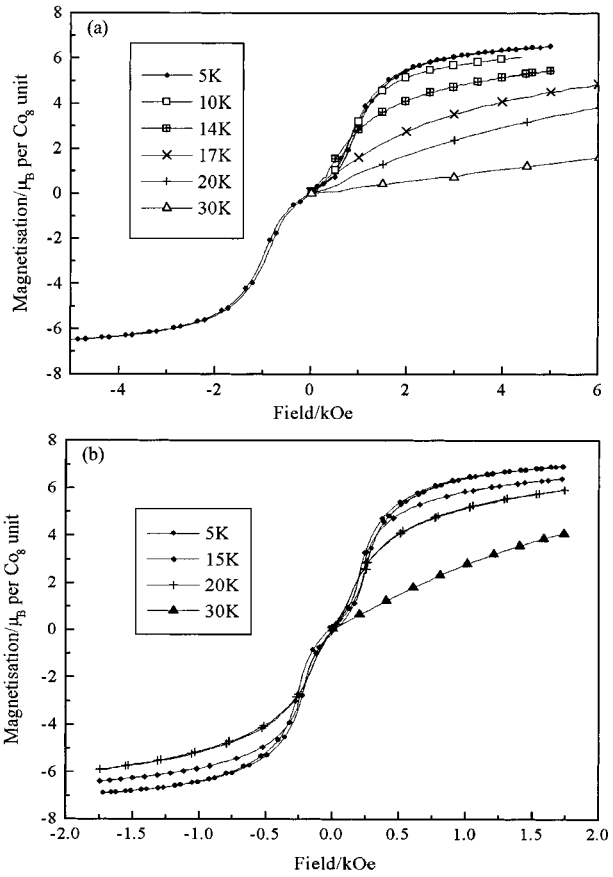

Figure 7. (a) Isothermal magnetization curves for CSEN at $5 \leq T/\mathrm{K} \leq 30$ displaying an S shape at temperatures lower than 14 K and (b) isothermal magnetization curves for CSDAB collected at temperatures between 5 and 30 K showing increased curvature with decreasing temperature.

paramagnetic behavior at high temperatures is similar for both compounds. The moment decreases to a minimum at 120 K before rising to a maximum at the critical temperatures (14 K for CSEN and 21 K for CSDAB). (Figure 6) The data can be fitted to the Curie−Weiss law for the temperature range 200−300 K with $C = 2.46$ cm^3·K/mol and $\theta = -25(1)$ K for CSDAB and $C = 2.43$ cm^3·K/mol and $\theta = -28(1)$ K for CSEN. (Table S3, Supporting Information) The magnetic moments derived from these Curie constant are 4.44 and 4.41 μ_B, respectively. These values are less than those expected for Co^{II} with total orbital angular momentum contribution through spin−orbit coupling ($\mu_{eff}/\mu_B = g_J[J(J+1)]^{1/2}$; $J = 9/2$), but larger than those with the orbital angular momentum completely quenched ($(\mu_{eff}/\mu_B = 2[S(S+1)]^{1/2}$; $S = {}^3/_2$), which are 6.54 and 3.87 μ_B per Co, respectively. This suggests that the orbital contribution is incompletely quenched as normally observed for octahedral Co^{II}. Figure S5 (Supporting Information) shows data in the paramagnetic region collected up to 400 K on both CSDAB and CSEN: the loss of the interlayer water molecules does not affect the magnetic moment in the Curie−Weiss region but introduces considerable changes in the low-temperature magnetic behavior which will be addressed in a subsequent publication.

For CSEN, nonreversibility is observed in the ZFC/FC magnetization in an applied field of 0.58 Oe, with a bifurcation point at the peak in the magnetization at 14 K. The nonreversibility may arise from a small canting of the moments such that the resultant magnetization is lower than the total susceptibility at the Néel temperature (T_N). Such a situation has been seen in the layered $Co_2(OH)_2$(dicarboxylate) phase.[37−38] These systems consist of cobalt hydroxide layers, which are composed of antiferromagnetically coupled ferromagnetic chains. The low-field antiferromagnetic ground state in the present case may be derived from antiparallel alignment of ferrimagnetic layers. The ferrimagnetism within the layers arises from the moments at all octahedral sites being parallel and at all tetrahedral sites being antiparallel to the octahedral sites. The real component of the ac susceptibility reflects the warming curve of the ZFC/FC data and the imaginary part shows a very weak peak ($<{}^1/_{100}$ of the magnitude of the real part) below T_N for CSEN. In the higher dc applied field of 1000 Oe, the susceptibility saturates at ∼17 cm^3/mol.

Magnetization isotherms of CSEN (Figure 7a) are linear with field for temperatures well above T_N. As the temperature approaches T_N from above, the magnetization increases more rapidly at low fields, indicating an increasing correlation length within the layers. This situation is similar to that found for ferrimagnets due to the uncompensated moment present within the layers. Below the transition, the isotherms have the S-shape characteristic of a metamagnet, which is usually observed in layered compounds[39−43] due to the strong structural anisotropy producing anisotropy in and competitions between the exchange interactions. The metamagnetic critical field, defined as the low-field onset of curvature in the S-shaped magnetization isotherm, increases to a limiting value of 500 Oe on decreasing temper-

(37) Kurmoo, M.; Kumagai, H.; Green, M. A.; Lovett, B. W.; Blundell, S. J.; Ardavan,A.; Singleton, J. *J. Solid State Chem.* **2001**, *159*, 343.
(38) Kurmoo, M.; Kumagai, H. *Mol. Cryst. Liq. Cryst.*, in press.
(39) Stryjewski, E.; Giordano, N. *Adv. Phys.* **1977**, *26*, 487.
(40) Takada, T.; Bando, Y.; Kiyama, M.; Mitamoto, K. *J. Phys. Soc. Jpn.* **1966**, *21*, 2726.
(41) Day, P. *Acc. Chem. Res.* **1988**, *211*, 250.
(42) Bruinsma, R.; Aeppli, G. *Phys. Rev.* **1984**, *B29* (5), 2644.
(43) Broderick, W. E.; Thompson, J. A.; Hoffman, B. M. *Inorg. Chem.* **1991**, *30*, 2958.

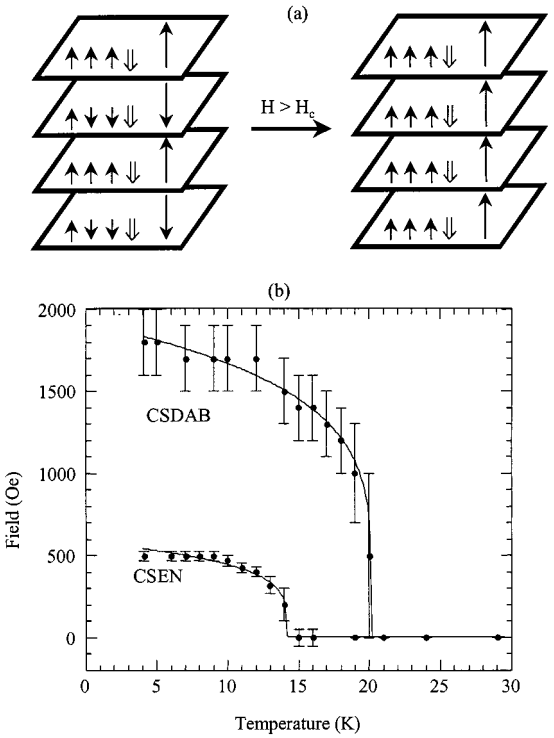

Figure 8. (a) Diagram showing the interlayered metamagnetic transition in increasing field above the critical field in CSDAB and CSEN. The moments of Co^{oct} and Co^{tet} are represented by filled and open arrows respectively, and the long arrows indicate the resultant moments in each layer, and (b) phase diagram for the T−O−T layered metamagnets. The experimentally observed critical field for the metamagnetic transition after zero-field cooling is shown as dots, and the fits to $H_c(T) = H_c(0)$. $((T_N - T)/T_N)^\beta$ are shown as solid lines. The derived parameters are given in the text.

ature. At 2 K, the saturation magnetization in a field of 50 kOe is 8.4 μ_B per Co_8 formula unit. For Co^{II}, the effect of spin−orbit coupling is usually to yield a Kramers $S = {}^1/_2$ state at low temperature[44] with an anisotropic *g*-tensor and a moment of 2.2 μ_B per Co^{II}. The observed saturation moments for the Co_8 unit in both CSDAB and CSEN are therefore equivalent to the resultant moment of four Co^{II}, assuming an effective $S = {}^1/_2$ at low temperatures. There are several possible ferrimagnetic layer configurations to yield this total moment, the simplest being ferromagnetically aligned octahedral sites (⇑⇑⇑) antiferromagnetically coupled to the tetrahedral sites (⇓), yielding an effective moment of four Co^{II} cations per Co_8 unit (Figure 8a). The exchange between the layers mediated by ethylenediamine is antiferromagnetic but weak and thus readily overcome by the applied field, producing the observed metamagnetic behavior in which the saturation moment when all the ferrimagnetic layers are aligned in parallel is that predicted by the simple model. The low coercivity indicates that the moments lie parallel to the layer.

Field-dependent molar susceptibilities and magnetizations of CSDAB are summarized in Figures 6b and 7b. The ZFC/FC data also display a sharp kink at 21 K due to the above-mentioned canting. The imaginary part of the ac susceptibility shows a very sharp but again weak peak at T_N. In CSDAB, the canting angle is larger than in CSEN, resulting in a sharp increase in the magnetization at T_N. On increasing the applied field, there is a gradual decrease in the susceptibility due to saturation effects. The overall ground state is similar to CSEN and appears to be antiferromagnetic in low field. The transition temperature is slightly higher than for CSEN, in good agreement with what is expected for a system where the layers are connected by a ligand that has three available pathways (DABCO) for magnetic exchange compared to another with only one (ethylenediamine). The small increase also suggests the interlayer magnetic exchange coupling through the pillars is weak.

The temperature dependence and the low-temperature saturation value of the isothermal magnetization for CSDAB are similar to those of CSEN. However, CSDAB exhibits a higher critical field for the metamagnetic transition. This again confirms the larger interlayer exchange in CSDAB. Most importantly, it demonstrates that through-bond exchange via the pillars is more likely to be the interlayer exchange mechanism rather than through-space (dipolar) coupling. The isotherms in both cases allow the H_c-T phase diagram for CSEN and CSDAB (Figure 8b) to be deduced. Fits to the critical exponent function (1)

$$H_c(T) = H_c(0)((T_N - T)/T_N)^\beta \qquad (1)$$

gave the following parameters for CSEN, $H_c(0) = 580 \pm 20$ Oe, $T_N = 14.2(2)$ K, and $\beta = 0.22(2)$; and for CSDAB, $H_c(0) = 1900 \pm 200$ Oe, $T_N = 20.2(2)$ K, and $\beta = 0.20(4)$.

Table 4. Summary of the Hydrogen Bond Analysis for CSDAB and CSEN Classified According to Type of Interactions[a]

		distance/Å	
interaction type	donor···acceptor	in CSDAB	in CSEN
host−host	O(1)···O(4)	3.07(1)	3.23(1)
	O(2)···O(4)	2.83(1)	2.78(1)
pillar−host	C(1)···O(4)	2.49(1)	***3.58*(*3*)**
host−guest	O(1)···O(7)	3.34(2)	
	O(1)···O(11A)		3.49(8)
	O(1)···O(11B)		3.40(8)
	O(1)···O(11C)		2.76(8)
	O(4)···O(11A)		2.92(2)
	O(4)···O(11B)		2.73(2)
	O(4)···O(11C)		2.67(2)
	O(4)···O(7)	3.45(2)	
pillar−guest	C(1)···O(7)	***3.59*(*1*)**	
	N(1)···O(7)	***4.79*(*1*)**	
	C(1)···O(11C)		2.64(7)
	N(1)···O(11A)		3.11(8)
	N(1)···O(11B)		3.40(8)

[a] O(7) denotes the water in CSDAB, and O(11A), O(11B), and O(11C) denote the disordered water in CSEN. The interactions that are too long to contribute to the hydrogen-bonding network are shown in italica for comparison.

Discussion

The DABCO and ethylenediamine pillars in these layered T−O−T frameworks allow the structure to be maintained upon loss of the interlayer guests. The differing conformational flexibility of the two pillars, however, leads to quite different structural behavior upon dehydration. To understand this, it is first important to consider the details of the as-grown hydrated structures.

The analysis of hydrogen bonds in both CSDAB and CSEN is summarized in Table 4 and Figure 9. In Table 4, the hydrogen bonds are classified into four different types of interactions, i.e., host−host, pillar−host, host−guest, and pillar−guest. The larger size of the DABCO molecule compared to the ethylenediamine pillar constrains the orientation of the nearby sulfate pendant in the CSDAB structure. The hydrogen-bonding network between the pillars and the sulfate groups in the CSDAB and

(44) de Jongh, L. J., Ed. ***Magnetic Properties of Layered Transition Metal Compounds***; Kluwer Academic Publishers: Dordrecht, The Netherlands, 1990.

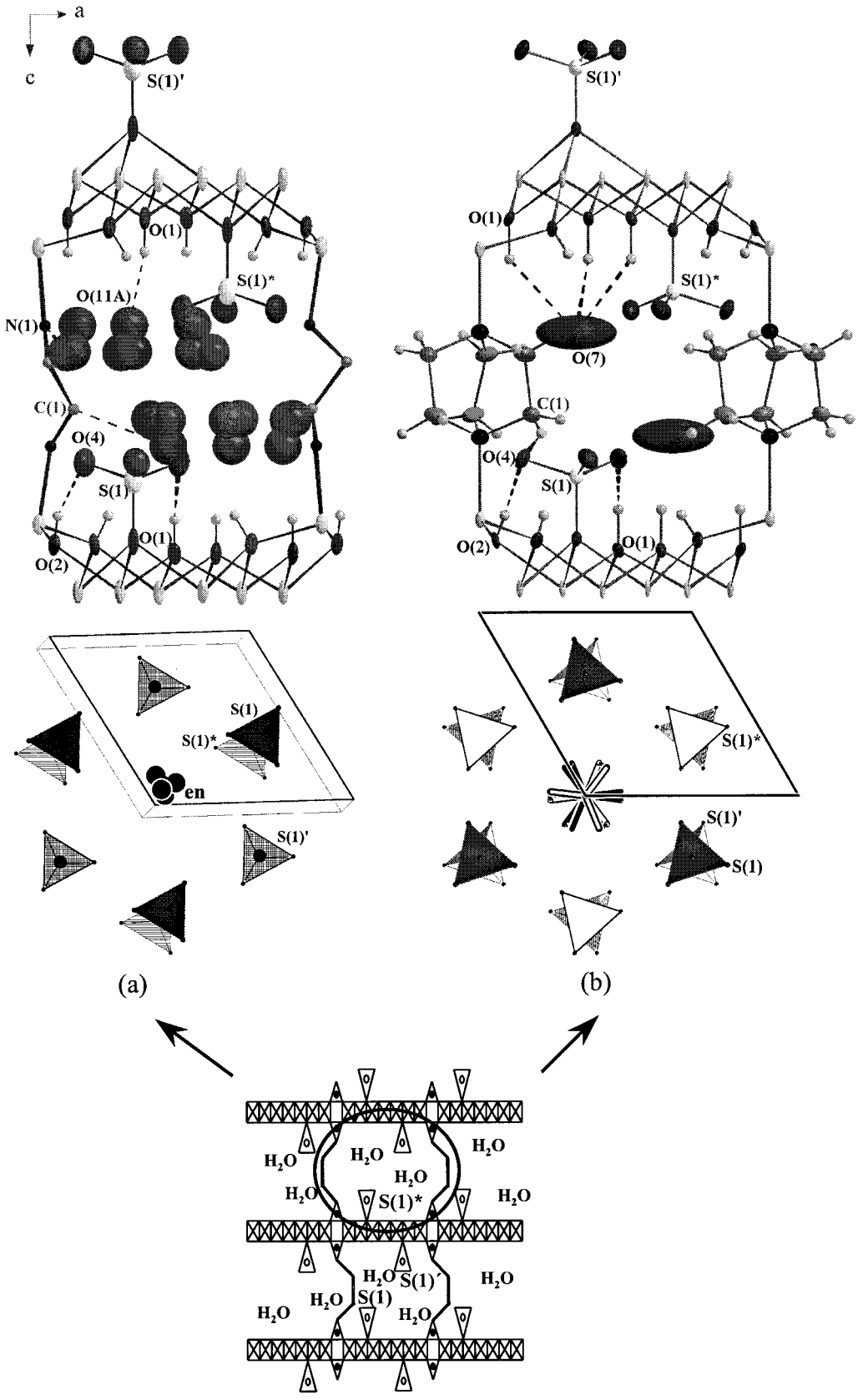

Figure 9. View along the *b* axis of the hydrogen-bonding network (dashed line) in (a) CSEN and (b) CSDAB. The correlation between the orientations of vertically adjacent sulfates and also diamine pillars are shown, demonstrating the differences between the AAA and ABA layer arrangements; S(1) is the sulfate on the top of one layer, and S(1)* and S(1)′ represent those on the bottom of this layer and the top of the next adjacent layer. In CSDAB, the torsion angle between the $S(1)O_4$ and $S(1)'O_4$ units is 36.1° whereas this angle is 0° in CSEN.

CSEN compounds is therefore different, although the intra-host hydrogen bonds, i.e., between layer hydroxides and the sulfate basal oxygens, are similar in both cases. The larger DABCO molecule is close enough to the sulfate group to form

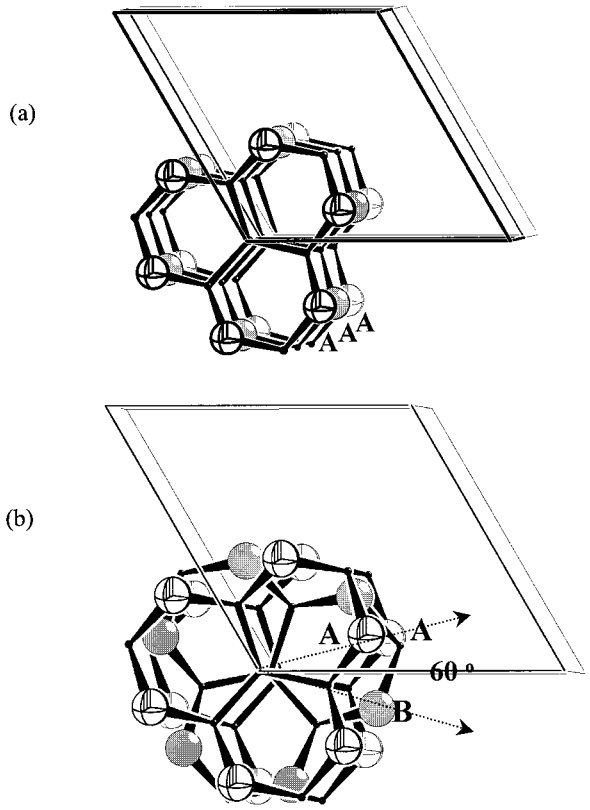

Figure 10. Perspective views along the *c* axis of the different arrangements of adjacent metalhydroxide host layers in (a) CSEN and (b) CSDAB. Circles represent Co^{oct} atoms. The different orientations of successive layers are correlated with the pillar and sulfate orientations shown in Figure 9.

C−H···O hydrogen bonds with the sulfate basal oxygen atom. This hydrogen bonding and the steric influence of the DABCO determine the orientation of the sulfate group, resulting in the rotation of the sulfate anions by 23.9° between the top of one layer and the bottom of its neighbor (the torsion angles between S(1)−O(4) and S(1)*−O(4) are shown in Figure 9b). The smaller ethylenediamine pillar in CSEN does not interact with the sulfate pendant either sterically or by hydrogen bonding. The sulfate groups in the CSEN structure are thus allowed to optimize their hydrogen-bonding environments and adopt a different orientation, with the corresponding torsion angle between two sulfate groups on the top and bottom of the adjacent layers of 60° (S(1) and S(1)* in Figure 9a). The layer orientation is strongly correlated with the orientation of the sulfate groups by the hydrogen bonds to the framework hydroxides. The differing sulfate orientations in CSDAB and CSEN therefore produce different layer orientations and consequently alter the layer registry. CSEN adopts an AAA layer arrangement (Figure 10a), where successive layers are perfectly superimposed. The adjacent layers in the CSDAB structure (Figure 10b), and also the DABCO pillars (Figure 9b), are related by 60° rotation, which superimposes the third layer on the first to give an ABA layer arrangement and the almost doubling of the *c*-axis in CSDAB.

The sequence of species liberated from the CSDAB and CSEN frameworks on heating is alike, i.e., water of crystallization, sulfate pendants, and then the organic pillars. In situ X-ray diffraction at high temperature shows that the CSDAB framework retains crystallinity up to 360 °C (decomposition begins at 320 °C), where TGA-MS data show that the sulfate groups are lost, demonstrating the key role of these anions in stabilizing the structure. CSEN totally collapses at a lower temperature (Figure 4; 320 °C). The differing behavior on guest loss can be attributed to the difference in rigidity between the organic pillars, but the ultimate difference in thermal stability must arise from differences in sulfate−pillar interactions, as the sulfate group in CSDAB structure also forms hydrogen bonds to the DABCO pillar, which is not found in the CSEN framework (Table 4). It might have been expected that the frameworks would only collapse upon the loss of the organic pillars rather than the sulfate groups. The key role of the sulfate units in stabilizing the structure does, however, tie in with the strong correlation between organic pillar and sulfate orientation already noted, suggesting that sulfate−hydroxide interactions ultimately control the stability of the inorganic layers themselves, which surprisingly decompose before the organic pillars linking them. New pillar−oxyanion combinations may therefore afford yet more stable structures.

The sulfate groups in CSEN form hydrogen bonds with the water of crystallization (pillar−guest in Table 4). The DABCO molecule, which is ∼3 times the size of ethylenediamine, occupies a much greater volume so that less water of crystallization is present in the reduced (5% vs 16.5% for CSEN) solvent accessible volume. The interstitial water in CSDAB, in contrast to CSEN, is closer to the framework rather than the DABCO molecules as a result of the increased steric hindrance and more hydrophobic nature of the neighboring pillars. The contacts formed between the water and the framework (particularly the sulfates) are long compared to the corresponding interactions in CSEN. The interlayer water molecules in CSEN are also located close to the ethylenediamine pillars, which allows hydrogen bonding with the primary amine group. The disorder of the ethylenediamine about the 3-fold rotation axis leads to significant disorder in the position of the hydrogen-bonding water via these interactions. In addition, the methyl groups of the ethylenediamine can form weak hydrogen bonds to the water molecules (pillar−guest in Table 4), according to the criteria of Steiner and Saenger[45] (C−H···O < 2.8 Å and D−H···A > 90° where D and A are hydrogen donor and acceptor, respectively). It is worth noting that the interlayer regions are chiral but that the neighboring interlayer regions alternate in their handedness because the opposite sides of the cobalt hydroxysulfate layer, which has inversion symmetry, have opposite chiralities.

The three-dimensional structure of the CSDAB framework is maintained and stabilized by the intralayer hydrogen bonding between the hydroxyls and sulfate oxygen atoms after dehydration. A higher temperature is required to yield the fully dehydrated phase (**2** in Figure 3) in the case of CSEN (260 °C) according to TGA and in situ X-ray diffraction. This may be due to enhanced guest−host hydrogen bonding in **2***, where the interlayer separation is considerably reduced as 50.6% of the guest is thermally expelled at 80 °C. (Figure 4) In addition, only the 00*l* reflections are observed above this temperature. This is due to the loss of correlation between the T−O−T layers in the *x* and *y* directions, which results from the tilting of the flexible ethylenediamine pillars and a slippage of the layers relative to each other. The retention of the 00*l* reflections indicates that the interlayer separation and its long-range coherence along *c* are maintained upon the loss of water. The interlayer spacing continues to reduce on further heating until the fully dehydrated state **2** is attained. In contrast, DABCO, with the rigid structure of the triply bridged ring, cannot change its conformation. Consequently, no dramatic change to the cell

(45) Steiner, T.; Saenger, W. *J. Am. Chem. Soc.* **1993**, *115*, 4540.

parameters is observed upon the loss of the interlayer water from CSDAB. The small observed expansion along *c* in CSDAB on guest desorption may be due to the increased thermal motion of the DABCO pillar, which is likely to exchange between its two propeller forms at higher temperatures.

The magnetic behavior of both phases arises from the dominant intralayer antiferromagnetic coupling between two sublattices ($3Co^{oct}$ and $1Co^{tet}$) producing a minimum in the temperature dependence of the moment. At a lower temperature, the maximum in the susceptibility is observed, which is interpreted as long-range antiferromagnetic (AF) ordering. The intralayer correlations are the sum of all the Co−O−Co exchange pathways and can be expected to be frustrated by the triangular geometry of the layers. They remain stronger than the interlayer antiferromagnetic coupling mediated by the ethylenediamine bridges.

The magnetically ordered state displays irreversibility between FC and ZFC magnetization. The S-shaped magnetization isotherms, which in both cases saturate at $\sim 1\ \mu_B$ per Co, indicate a metamagnetic transition to a ferrimagnetic-like state on increasing the field. In zero field, the presence of both octahedral and tetrahedral Co^{II} centers may produce more than two antiferromagnetic sublattices, and the associated canting will produce domain effects giving rise to the FC/ZFC hysteresis: the isotherms and the ac susceptibility data both argue against a spin-glass interpretation. Large hysteresis is typically observed for layered magnets when the easy axis is perpendicular to the layer and has been demonstrated to occur for metamagnets and ferrimagnets based on layered cobalt hydroxides.[17,18,35]

The ZFC AF ground state is transformed to a ferrimagnetic state on application of a field large enough to overcome the interlayer AF coupling. The saturation value ($\sim 8\mu_B$ per Co_8) can be interpreted as ferrimagnetic alignment of Co^{II} ions with a highly anisotropic *g*-tensor arising from strong spin−orbit coupling giving rise to a Kramers doublet $S = {}^1/_2$ ground state at low temperature. This then leads to an interpretation of the ground state below the critical field as ferrimagnetic sheets coupled antiferromagnetically by the interlayer exchange, which is weak (but required for three-dimensional ordering) and overcome by the applied field beyond H_c (Figure 8a). The enhanced critical field required for the metamagnetic transition in CSDAB and its higher transition temperature is related to the increased number of interlayer exchange pathways through the DABCO compared to en.

The phase diagram in Figure 8b shows that both CSDAB and CSEN display the same critical exponent within error for the metamagnetic transition. The value of this exponent, $\beta = 0.23$, derived for the metamagnetic critical field is very similar to the magnetization critical exponent associated with two-dimensional XY systems rather than the Ising behavior expected from the large single-ion anisotropy of Co^{II}. This exponent may therefore be consistent with the indication from the low coercive field that the moments lie in the planes of the cobalt hydroxysulfate layers.

Conclusion

This paper covers a family of porous magnetic materials whose structures and thermal stability can be tuned via the organic pillar and its interactions with the compositionally complex inorganic layer. The more rigid DABCO ligand produces a pillared metal hydroxysulfate layered structure that has higher thermal stability than its ethylenediamine analogue; it also retains three-dimensional structural ordering upon guest loss. The key role of the sulfate group in stabilizing these organo-pillared structures was revealed by TGA-MS. The magnetism of the layered cobalt hydroxide compounds is complex due to the influences of multiple metal sites, inter- and intralayer exchange, spin−orbit coupling, and geometrical frustration. The interlayer exchange mediated by the organic pillars drives zero-field antiferromagnetism but is sufficiently weak to allow a field-induced transition to a metamagnetic state. A synthetic route leading to a smaller number of tetrahedral metal sites would lead to larger pore volumes and is an important future goal, as is the detailed understanding of the complex magnetism of these triangular systems. The potentially wide variation in pillar, oxyanion, and multiple ordered metal occupancy at the octahedral and tetrahedral sites makes future synthetic exploration of these new porous magnetic phases an interesting prospect.

Acknowledgment. A. R. thanks the Royal Thai Government for a graduate scholarship and Dr. M. Bieringer (Institut Laue Langevin, France) for useful discussion. H.K. and M.K. thank the CNRS and JSPS for funding. The UK EPSRC provided access to Station 9.8 at the Daresbury SRS.

Supporting Information Available: Additional information as noted in the text (refined parameters for CSDAB, CSEN structural figure, UV-visible and FTIR spectra for both phases, high temperature magnetisation data, additional TGA-MS data). This material is available free of charge via the Internet at http://pubs.acs.org.

JA0109848